Polymer Bulletin
https://doi.org/10.1007/s00289-025-05923-z

ORIGINAL PAPER

Rheological optimization of hybrid alginate–xanthan gum hydrogels for enhanced 3D bioprinting fidelity

Lizardo K. Torres-Ayala[1,2] · Javier Nakamatsu[3] · Suyeon Kim[2]

Received: 14 May 2025 / Revised: 18 June 2025 / Accepted: 23 June 2025

Abstract

This study presents a systematic and reproducible methodology for the development and evaluation of hybrid hydrogels tailored for extrusion-based 3D bioprinting. To demonstrate the applicability of this approach, alginate and xanthan gum were selected as model materials, two of the most widely reported polymers in the biofabrication literature. Rather than relying on empirical trial and error, the methodology integrates material screening, rheological and chemorheological analyses, predictive modeling, and experimental validation to address key challenges in reproducibility, print fidelity, and structural stability. The AL_4XA_4 formulation emerged as a robust candidate, exhibiting shear-thinning behavior, rapid thixotropic recovery, and adequate mechanical strength to maintain filament integrity during extrusion. Power-law-based modeling enabled the rational adjustment of extrusion pressures and nozzle configurations, leading to consistent deposition with minimal defects. Although no living cells or biological additives were used, bioprinting protocols were applied to assess printability and structural performance. The material formed self-supporting filaments with unsupported spans up to 6 mm. Chemorheological testing confirmed the reinforcing effect of ionic cross-linking (1.5–3% $CaCl_2$) in enhancing construct stability. This framework offers a transferable strategy for standardized bioink development and structural benchmarking, paving the way for reproducible biofabrication in tissue engineering and related biomedical applications.

Keywords Three-dimensional bioprinting · Hybrid hydrogels · Alginate · Xanthan gum · Rheological optimization · Scaffold fabrication · Tissue engineering · Direct Ink Writing (DIW)

✉ Suyeon Kim
skim@pucp.edu.pe

[1] Master's Program in Materials Science and Engineering, Pontificia Universidad Católica del Perú-PUCP, Lima, Peru

[2] Department of Engineering, Pontificia Universidad Católica del Perú-PUCP, Lima, Peru

[3] Chemistry Division, Department of Science, Pontificia Universidad Católica del Perú-PUCP, Lima, Peru

Published online: 11 July 2025

Abbreviations

AL	Alginate
XA	Xanthan gum
PR	Printability ratio
n	Flow behavior index
K	Consistency index
μ	Viscosity
σ_y	Yield stress
$h_{\max}$	Maximum printable height
t_s	Gelation time
TDS	Time-dependent solidification
STL	Standard tessellation language
CAD	Computer aided design
FDM	Fused deposition modeling
R_1	Nozzle radius
ΔP	Pressure drop
Q	Volumetric flow rate
ρ	Density
τ	Shear stress
$\dot{\gamma}$	Shear rate
η_0	Plastic viscosity
DIW	Direct ink writing
C_f	Collapse factor
G-code	Geometric code

Introduction

The swift advancement of three-dimensional printing technologies tailored for viscoelastic materials has revolutionized the field of tissue engineering, facilitating the fabrication of complex structures pertinent to applications including cartilage repair and organ scaffolding. However, designing bioinks that balance biocompatibility, biodegradability, and mechanical stability while maintaining the structural precision required for complex tissue constructs remains a significant challenge [1–3].

The optimization of specific rheological properties, including shear-thinning behavior, yield stress, and thixotropic recovery, is crucial for achieving successful bioprinting. These properties ensure stable extrusion and preserve construct geometry during the printing process. For example, insufficient yield stress may result in filament collapse, thereby compromising structural integrity. Hybrid hydrogels, which integrate the properties of multiple polymers, offer a promising strategy to address these challenges by allowing for the precise adjustment of rheological profiles [4].

While several studies have extensively characterized the gelation process and optimized the extrudability of various hydrogel formulations [5–7], a key limitation persists: the lack of standardized and reproducible methodologies to evaluate printability and structural fidelity under unsupported conditions. This gap hinders

comparative analysis and reliable implementation across different material systems, highlighting the need for systematic frameworks that correlate rheological behavior with structural outcomes [8].

Hybrid hydrogels, such as alginate–xanthan gum formulations, represent a unique approach to overcoming these challenges by combining the shear-thinning behavior and mechanical stability of alginate with the elasticity and structural reinforcement provided by xanthan gum [9]. Unlike single-polymer systems, hybrid hydrogels enable tailored rheological profiles that facilitate extrusion while maintaining integrity in multi-layered, unsupported configurations. However, integrating material characterization with process optimization is critical to bridge the gap between material development and reliable structural performance [4].

In this context, the present study does not aim to introduce a new material per se, but rather proposes a demonstrative framework for evaluating structural performance in hybrid hydrogels. While the AL-XA system was selected as a model due to its robustness and accessibility, the methodology presented here centered on self-supporting capacity, collapse quantification, and chemorheological behavior is readily adaptable to other bioinks.

Hybrid hydrogels: leveraging individual properties to achieve novel functionalities

Bioprinting is a method used in tissue engineering that deposits bioinks layer by layer to construct tissue structures. It offers advantages over traditional techniques, such as lyophilization and electrospinning, by improving reproducibility and control in fabricating biological models [10]. A central challenge remains the development of bioinks that meet the mechanical, biological, and rheological requirements of bioprinting. Pedroza et al. highlighted that although material innovations address specific issues, many still lack clinical applications, particularly for complex organs like kidneys, which need architectures that current bioprinting technology cannot achieve [11].

Hydrogels are widely used in bioprinting due to their ability to form networks that support cell growth and 3D structures [11, 12]. As scaffolds, they are appealing because they mimic the extracellular matrix, are processable under mild conditions, and can be delivered minimally invasively. These properties make hydrogels ideal for applications in tissue engineering, including drug delivery, cellular organization, and stimuli-responsive systems [12]. However, when used individually, they often lack essential properties such as mechanical strength, cell adhesion, and proper rheological behavior for advanced applications [13, 14].

Alginate (AL), an anionic polysaccharide derived from brown algae, is one of the most widely used base materials in extrusion-based bioprinting due to its shear-thinning behavior, biocompatibility, and ionic cross-linking capacity with divalent cations such as Ca^{2+} [11, 15, 16]. Nevertheless, its poor cell adhesion and limited mechanical strength have motivated extensive research into composite strategies. Numerous studies have explored hybrid formulations by blending alginate with gelatin, κ-carrageenan, or other polymers to improve printability, elasticity, and

biological performance, enabling the fabrication of viable and functional constructs for diverse biomedical applications [17–19].

Xanthan gum (XA), a bacterial polysaccharide, has also emerged as a valuable additive to modulate viscoelastic properties and improve extrusion fidelity, although it lacks inherent structural integrity post-cross-linking. The combination of AL and XA has shown promise in creating printable hydrogels with balanced mechanical and rheological properties [15].

Rheological optimization for hybrid hydrogels in 3D bioprinting

Rheology is fundamental to understanding how hydrogels behave under stress during extrusion in bioprinting[20, 21]. The rheological properties of a bioink directly impact its ability to flow through the nozzle, form continuous filaments, and maintain structural integrity upon deposition. Shear-thinning materials, whose viscosity decreases with applied shear, are particularly critical for ensuring smooth extrusion and precise filament formation [15, 20, 21].

Maintaining a stable flow rate and precise material deposition is essential in bioprinting. The volumetric flow rate (Q) must synchronize with the print head's speed to produce uniform layers without deformation or collapse [22]. Rheological models, such as the power-law model, effectively describe the flow behavior of non-Newtonian fluids such as AL and XA hydrogels, which exhibit pseudoplasticity (i.e., viscosity decreases with increasing shear). Controlling these properties is critical for optimizing print fidelity and structural stability [21].

Hybrid hydrogels composed of AL and XA exemplify tunable pseudoplastic behavior, offering the ability to balance yield stress and flow properties. Achieving this balance ensures smooth extrusion and stable post-printing structures. This study applies classification frameworks proposed by Rau et al., which categorize materials based on yield stress and time-dependent solidification, to enhance the printability and reliability of extrusion-based constructs [22].

Enhancing precision and structural integrity with viscoelastic materials in 3D printing

Three-dimensional printing is structured around three core stages: preprocessing, processing, and post-processing. It begins with a conceptual design, often derived from digital blueprints or real structures captured via 3D scanning, MRI, or CT, which form the foundation for creating a three-dimensional model ready for fabrication [10, 23]. During the preprocessing phase, careful material selection, tailored to the specific application, is essential—such as using hybrid hydrogels combining beta-tricalcium phosphate (β-TCP) with biopolymers like collagen or gelatin to mimic the inorganic components of bone tissue in bioprinting bone models [24].

Direct Ink Writing (DIW), a technique closely aligned with 3D bioprinting, offers precision in the fabrication process by using a pressure-controlled system that deposits material layer by layer without requiring heat. This method provides flexibility in processing a wide range of materials and involves three key subfunctions: extrusion,

solidification, and layer support. During extrusion, a pressure gradient is applied to initiate material flow, while internal shear forces regulate filament continuity and stability [22]. Solidification transitions the material from a viscous state to a stable structure with acceptable deformation, while layer support ensures that the printed material bears the weight of subsequent layers without collapsing or deforming, maintaining structural integrity throughout the build process [22, 25].

The creation of three-dimensional models relies on CAD software to generate a mesh representation, typically exported in STL format, which outlines the surface geometry but lacks material and physical properties required for direct 3D printing, and slicer software, such as Slic3r or Simplify3D, then converts this STL file into G-code, an operational protocol for printers used to fine-tune printing parameters by dictating extruder movements and parameters like motor speed, ensuring accurate layer-by-layer fabrication [26, 27].

In this study, optimizing G-code was crucial for fine-tuning print parameters such as speed, pressure, and material placement, allowing for the precise adjustment of extrusion speed and pressure to control strand width; this directly impacted the structural and functional integrity of DIW-printed models with greater precision, offering flexibility that mitigated common issues such as over- and under-extrusion, thereby ensuring more consistent and reliable prints and maintaining print fidelity to match intended designs [26, 28–30]. An effective technique toward optimizing extrusion printing quality is also printing parameter optimization, as recent studies demonstrate how systematic tuning of these parameters can significantly improve printability and construct fidelity in extrusion-based processes [31].

To evaluate the precision and structural fidelity of the printed constructs, this study employed quantitative methods such as circularity algorithms and macropore fidelity analysis. Specifically, the Printability Ratio (PR), defined as a geometric function of macropore perimeter and area, was calculated from cross-hatched mesh patterns to assess deviation from the intended geometry. These metrics—further detailed in Section 2.8—were essential for ensuring that the printed structures retained their intended shape and pore architecture [32, 33].

Although this study focuses on optimizing the processing phase, post-processing is also crucial for maintaining the printed geometry and ensuring tissue viability. A key aspect of this work is the evaluation of the self-supporting capacity of the printed constructs, which is critical to ensure they can withstand gravitational forces without deformation. This is assessed through the Collapse Index, providing a quantitative measure of the scaffold's structural stability. Additionally, chemorheological evaluations and cross-linking with calcium chloride ($CaCl_2$) were performed to further improve the mechanical integrity and solidification behavior of the bioprinted constructs [34]. Constructs are typically maintained in bioreactors to ensure sterility and mechanical stability under optimal conditions, as established in prior studies, but these aspects are beyond the scope of the present work [35–37].

Materials and methods

Materials and equipment

Sodium AL (MKCF1224, Sigma-Aldrich, St. Louis, MO, USA) and XA (Bob's Red Mill, USA) were used as the primary components for the bioink formulation. Polylactic acid (PLA) was utilized for fabricating molds in the strand collapse tests using Fused Deposition Modeling (FDM). The bioprinting process was conducted using an Allevi 3 bioprinter (Allevi Inc., USA), equipped with 20 G and 22 G nozzles (inner diameters of 0.610 mm and 0.413 mm, respectively), along with Allevi syringes to ensure accurate extrusion of the bioinks. The printed structures were deposited onto plastic Petri dishes. Rheological properties, such as viscosity and viscoelastic behavior, were measured using an Anton Paar MCR 92 rheometer (Anton Paar, Austria). Calcium chloride ($CaCl_2$) was employed as the cross-linking agent to induce gelation of the sodium AL during and after bioprinting.

Preparation of hydrogels

AL and XA hydrogels were prepared individually in concentrations ranging from 0.5% to 8% (w/v) for alginate. Hybrid mixtures were also formulated to study the effect of adding xanthan gum: AL2XA1, AL4XA2, AL4XA4, AL4XA6, and AL6XA6. In each formulation name, the numbers indicate the concentrations (in %) of alginate and xanthan gum, respectively. For example, AL6XA6 corresponds to a formulation with 6% alginate and 6% xanthan gum.

All solutions were dissolved in deionized water under magnetic stirring for 8 h. During the first 40 min, the temperature was maintained at 60 °C to facilitate solubilization, particularly in highly viscous formulations such as AL6 and AL6XA6. A laboratory spatula was used to prevent powder from adhering to the walls of the vessel and to promote uniform dispersion. Stirring continued at room temperature for the remaining time.

The same preparation procedure was applied uniformly to all individual and hybrid formulations.

Preliminary manual extrudability assessment

Before proceeding with detailed rheological characterization and experimental bioprinting, a manual extrudability assessment was conducted to refine the selection of bioinks, based on a similar approach described by O'Connell [38], though adapted to meet the specific needs of this study. This step allowed us to limit the number of formulations evaluated, thereby enhancing the efficiency of the optimization process. Each bioink was carefully loaded into syringes, ensuring the absence of air bubbles, and extruded through 22 G and 20 G nozzles. The goal was to achieve smooth, uninterrupted extrusion, while preventing material

leakage or clogging at the nozzle tip. Additionally, we ensured that the extruded material retained its shape without excessive spreading.

This initial assessment was crucial for identifying potential printability issues early on, ensuring that only formulations with adequate flow properties advanced to subsequent rheological and bioprinting tests.

Rheological characterization and extrusion parameters

In accordance with the rheological roadmap proposed by Rau et al. [22], a rotational flow sweep was performed to analyze the material's response to varying shear rates, focusing on yield stress materials and those exhibiting time-dependent solidification. The experiments utilized an Anton Paar MCR92 rheometer with parallel plate geometry (1 mm gap), where the shear rate was logarithmically ramped from 0.01 s^{-1} to 100 s^{-1}, producing a comprehensive viscosity profile over a broad range.

The material's non-Newtonian behavior was described using the *Power-Law model*, which relates shear stress (τ) to shear rate ($\dot{\gamma}$):

$$\tau = K \cdot \dot{\gamma}^n \tag{1}$$

Here K represents the consistency index, while n denotes the flow behavior index [21]. These parameters were extracted from the experimental data using Python (version 3.10) with the NumPy and SciPy libraries for data processing and curve fitting.

Using the extracted parameters, the extrusion pressure for bioprinting was estimated through the pressure drop equation for cylindrical nozzles:

$$\Delta P = 2KL_1R_1^{-(3n+1)}\left(\frac{Q \cdot (3n+1)}{\pi n}\right)^n \tag{2}$$

where L_1 is the nozzle length, R_1 is the nozzle radius, Q is the volumetric flow rate, and ΔP is the pressure drop [39, 40]. The volumetric flow rate was adjusted from 0 to 3 mL/min to simulate standard bioprinting syringe capacities. Materials requiring pressures beyond the bioprinter's operational capacity were deemed non-extrudable.

For yield stress characterization, the Casson model was employed:

$$\sqrt{\tau} = \sqrt{\tau_0} + \sqrt{\eta_0 \dot{\gamma}} \tag{3}$$

where τ_0 is the yield stress, and η_0 represents the plastic viscosity. This model effectively captures the initial resistance to flow and subsequent plastic flow behavior, offering critical insights into the material's printability.

The integration of these rheological analyses enabled a predictive understanding of material performance during extrusion, ensuring that the bioink met the mechanical and operational demands of the bioprinting process.

Oscillatory rheology: amplitude sweep assessment

To further investigate the viscoelastic properties of the alginate–xanthan gum hydrogels, an oscillatory amplitude sweep was performed. The strain amplitude was logarithmically increased from 0.01% to 100%, maintaining a constant angular frequency of 1 Hz. Both the storage modulus (G') and loss modulus (G'') were recorded to observe the transition from elastic (solid-like) to viscous (liquid-like) behavior.

The critical strain, defined as the point where G' significantly decreases, was identified as the material's yield point. This parameter is essential for ensuring printability and mechanical stability during extrusion.

Thixotropic recovery test

To evaluate the material's ability to recover its structure after yielding, a three-interval thixotropy test was conducted. The sample was initially subjected to high strain (10%) for 100 s to induce yielding, followed by a low strain (0.01%) for an additional 100 s to monitor recovery behavior. The percentage recovery was calculated as the ratio of the storage modulus (G') after the low-strain phase to its initial value, providing a quantitative measure of structural recovery.

This test is crucial for predicting the hydrogel's capacity to maintain its form between consecutive layers during 3D bioprinting, ensuring structural integrity throughout the printing process.

Optimization of bioprinting parameters: impact on extrusion speed and resolution

Bioprinting was conducted using a specifically selected bioink, which exhibited suitable rheological properties as determined by the tests performed in this study. A custom G-code was designed prior to printing, controlling extrusion speeds across multiple lines with varying velocities to optimize filament deposition in Allevi 3 bioprinter. This setup provided precise control over the extrusion process, bypassing the limitations of conventional slicer software [29, 30].

Pressure adjustments were programmed into the Allevi BIOPRINT PRO software, using ranges derived from rheological flow sweep data. These controlled variations in speed and pressure were crucial for maintaining consistent filament size and uniformity, which had a direct impact on extrusion resolution [5].

Filament dimensions were measured using ImageJ software, with triplicate samples taken to ensure accuracy and consistency. The collected data were processed and analyzed using Python, where trends were visualized to identify the optimal printing conditions.

Precision quantification in 3D printing of biomaterial inks: correlating circularity, gelation, and macropore fidelity

To engineer a precise and stable macroporous scaffold, we employed G-Code to design a cross-hatched mesh with adjustable spacing between horizontal and vertical strands. By systematically varying the distances between the strands, we generated macropores of different sizes, allowing us to evaluate printability precision (*PR*) using the circularity algorithm. This method, defined by the equation:

$$PR = \frac{L^2}{16A} \tag{4}$$

where L represents the perimeter and A the area of the printed macropores, was crucial for ensuring that the strands retained their structural integrity without merging or collapsing. The calculation of *PR* provided a quantitative measure of print fidelity, helping us maintain the distinct geometry of each macropore.

We carefully analyzed the *PR* values obtained from varying strand spacings to identify the optimal conditions for scaffold stability. Values exceeding 1 indicated a tendency for strand collapse, likely due to excessive spreading of the bioink. In contrast, *PR* values slightly below 1 suggested ideal gelation properties, where the bioink formed stable and well-defined macropores without excessive deformation. Our goal was to optimize the macropore dimensions to achieve a *PR* value close to, but slightly less than, 1—typically within the 0.85–0.98 range—thus promoting slight filament contraction upon deposition. This behavior improves pore definition and minimizes structural overlap, contributing to a scaffold architecture with high spatial fidelity and favorable conditions for tissue integration [32, 33].

Additionally, the pressure and velocities applied during the printing process were calibrated based on previous experiments to ensure consistency in material flow and structural stability.

Printability and layer support evaluation

The printability and structural stability of the AL4XA4 hydrogel formulation were assessed by evaluating both its solidification behavior and its ability to support multiple layers without deformation. The permissible gelation time (t_s) necessary to prevent strand spreading or collapse during extrusion was calculated using the following equation, adapted from Duty et al. [25]:

$$t_s \leq \frac{0.761\mu}{h_0 \rho g} \tag{5}$$

where μ represents the ink's viscosity, h_0 is the height of the extruded strand, ρ is the material's density, and g is the gravitational constant. This approach ensures that the hydrogel solidifies rapidly enough to maintain the printed structure without significant deformation during the extrusion process [22, 41]. Additionally, the yield stress (σ_y) was measured to estimate the maximum printable height ($h_{\max}$) the hydrogel could support before yielding, using the equation:

$$h_{\max} = \frac{\sigma_y}{\rho g} \tag{6}$$

This provided an estimation of the material's structural integrity, defining the maximum height that could be printed without deformation, ensuring mechanical stability during and after the extrusion process [42, 43]. A strand collapse test was conducted to further evaluate the material's structural integrity under gravitational forces. Hydrogel filaments were printed across gaps ranging from 1 mm to 6 mm using a custom fixture designed in *Autodesk Fusion 360*, with extrusion parameters adjusted via G-code. The Collapse Index (C_f) was used to quantify the structural collapse of the filaments, following the equation adapted from Habib et al. [44]:

$$C_f = \frac{A_{t_c} - A_{a_c}}{A_{t_c}} \times 100\% \tag{7}$$

where A_{t_c} is the theoretical area of the filament spanning the gap, and A_{a_c} is the actual area measured after collapse. A lower C_f indicates superior structural stability, with minimal deviation from the theoretical area. Each test was repeated three times to ensure reproducibility, and statistical analysis was conducted to confirm the consistency of the hydrogel's performance [45]. These evaluations provided critical insights into the hydrogel's mechanical properties, particularly its ability to span unsupported distances.

Chemorheological evaluation

The chemorheological evaluation aimed to characterize the cross-linking behavior of the AL4XA4 hydrogel using calcium chloride ($CaCl_2$) as an ionic cross-linker. Experiments were conducted with an Anton Paar MCR92 rheometer equipped with parallel plate geometry and a 1 mm gap. Oscillatory amplitude sweeps were performed to monitor the evolution of the storage modulus (G') and loss modulus (G'') during the cross-linking process. Two concentrations of $CaCl_2$ (1.5% and 3%) were tested, and cross-linking was initiated by introducing the $CaCl_2$ solution into the hydrogel via micropipette. The rheometer gap was recalibrated during the process to maintain consistent measurement conditions.

Post-extrusion cross-linking was assessed by fabricating a 3D ear model. The hydrogel was extruded in its uncross-linked state and cross-linked immediately after deposition by uniformly applying the $CaCl_2$ solution across the printed structure.

Results and discussion

Preparation and preliminary extrudability assessment of AL-XA bioinks

To initially assess the extrudability of various bioink formulations, concentrations of AL and XA ranging from 0.5% to 8% (w/v) were manually tested. AL-based bioink is the most extensively studied for extrusion-based bioprinting, and

Table 1 Manual extrudability assessment of bioink formulations

AL (%)	XA (%)	Outcome
0.5	0	Not printable
2	1	Not printable
4	2	Not printable
4	4	Printable
4	6	Printable
6	6	Syringe clogging
8	0	Not printable

their printability and structural stability can be improved by mixing other polymers [46, 47]. XA was introduced to improve not only cell adhesion but also the structural integrity of the bioink. Different concentrations of XA were incorporated progressively to observe its effects as a plasticizer and its influence on the bioink's extrudability. The outcomes are summarized in Table 1. In the initial experimental phase, the focus was on pure AL concentrations at the extremes of 0.5%–8%. These tests showed that both extremes led to poor printability, with the material either collapsing post-dispensing or failing to extrude properly due to improper viscosity. Printing with low viscosity ink results in the deformation and collapse, and the nozzle jamming occurs when high viscosity materials are printed [48].

The inclusion of 4% and 6% XA alongside 4% AL yielded printable bioinks capable of forming stable, continuous filaments. In contrast, the 6% XA and 6% AL mixture clogged the syringe, suggesting that excessive XA content leads to over-viscous formulations. These outcomes are visually summarized in Fig. 1.

As depicted in Fig. 1, the formulations containing 4% AL and 4–6% XA demonstrated consistent filament formation with limited spreading and no nozzle clogging during manual extrusion tests, which was instrumental in narrowing down bioink formulations for subsequent rheological and bioprinting experiments by identifying non-viable mixtures early on and optimizing the overall workflow to focus on formulations with the best printability and structural cohesion.

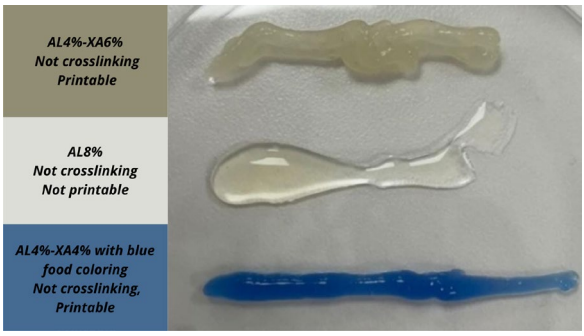

Fig. 1 Visual assessment and optimization of bioink formulations: dispensing dynamics illustrated on petri dish surfaces

Rotational flow sweep and rheological analysis

Rotational flow sweeps were employed to evaluate the viscosity (μ) of hydrogel formulations across a spectrum of shear rates ($\dot{\gamma}$), as delineated in the methodology. AL4 demonstrated an initial viscosity of 3.73 mPa·s at a shear rate of 0.01 s^{-1}, which markedly diminished to 0.255 mPa·s at a shear rate of 1000 s^{-1}.

The 4% XA (XA4) exhibited a substantial initial viscosity of 2215.81 mPa·s. This viscosity underwent pronounced shear-thinning, decreasing to 555.1 mPa·s at elevated shear rates. The shear-thinning behavior observed in both materials underscores their appropriateness for extrusion bioprinting applications, as it offers the requisite balance between flowability under pressure and stability at rest [49]. These results are illustrated in Fig. 2.

As the concentration of XA increased in the formulations, a corresponding increase in viscosity and a reduction in shear rate were observed [50], with the AL4XA4 blend showing a viscosity of 3136.5 mPa·s at a shear rate of 0.01 s^{-1}, decreasing to 555.1 mPa·s at 1000 s^{-1}, while the AL4XA6 blend exhibited even higher viscosity, starting at 6953.8 mPa·s at 0.01 s^{-1} and decreasing to 1187 mPa·s at 1000 s^{-1}, highlighting XA's role as a viscosity modifier that enhances the resistance of the material to flow, particularly at lower shear rates [50]. This relationship is shown in Fig. 3.

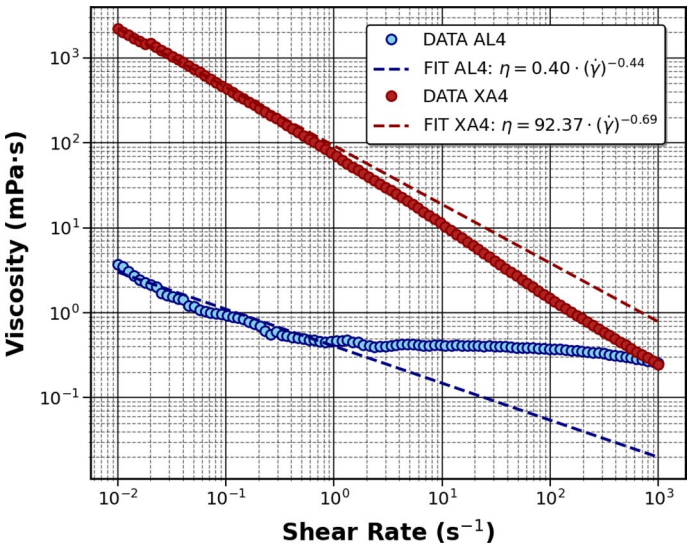

Fig. 2 Rotational Flow Sweep analysis of AL at 4% and XA at 4%. The graph shows the viscosity profiles for both materials, with noticeable shear-thinning behavior across the tested shear rates, demonstrating their potential for extrusion bioprinting

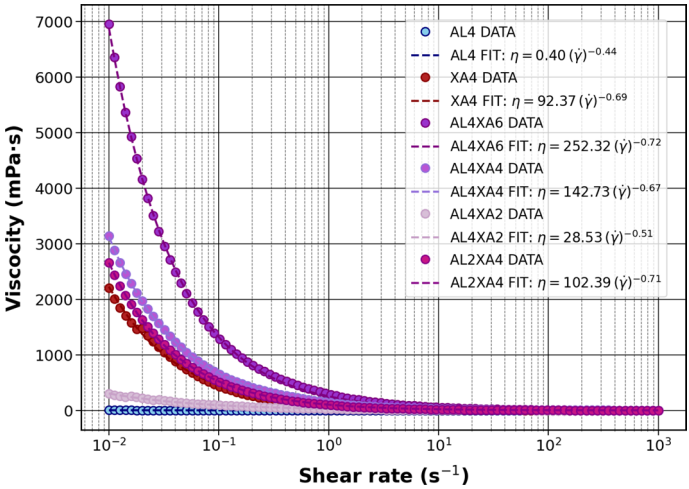

Fig. 3 Flow Sweep Analysis of increasing XA concentrations on the viscosity of hybrid hydrogels. The graph illustrates how XA enhances viscosity, particularly at low shear rates, while maintaining flowability at higher shear rates

Table 2 Consistency index (K) and flow behavior index (n) for hydrogel formulations, derived from the power-law model

Formulation	K (mPa·s)	n
AL4	0.40	0.56
AL2XA4	102.39	0.29
AL4XA2	28.53	0.49
AL4XA4	142.73	0.33
AL4XA6	252.32	0.28
XA4	92.37	0.31

Prediction of extrusion pressures using power-law parameters

The experimental data from the rotational flow sweeps were analyzed using the power-law model (Equation 2), yielding the consistency index (K) and flow behavior index (n) for each hydrogel formulation. These rheological parameters, shown in Table 2, are essential for understanding the material's behavior under shear. Specifically, K represents the material's viscosity at a specific shear rate, while n describes the degree of shear-thinning, indicating how much the viscosity decreases as the shear rate increases.

Using these parameters, the extrusion pressures required for each formulation were estimated by applying Equation 2, which integrates K, n, nozzle geometry, and volumetric flow rates (Q). The volumetric flow rates tested ranged from 0 to 3 mL/min, a range typical in extrusion-based 3D bioprinting. These calculations ensured that the predicted pressures aligned with practical printing conditions, enabling smooth and consistent material deposition.

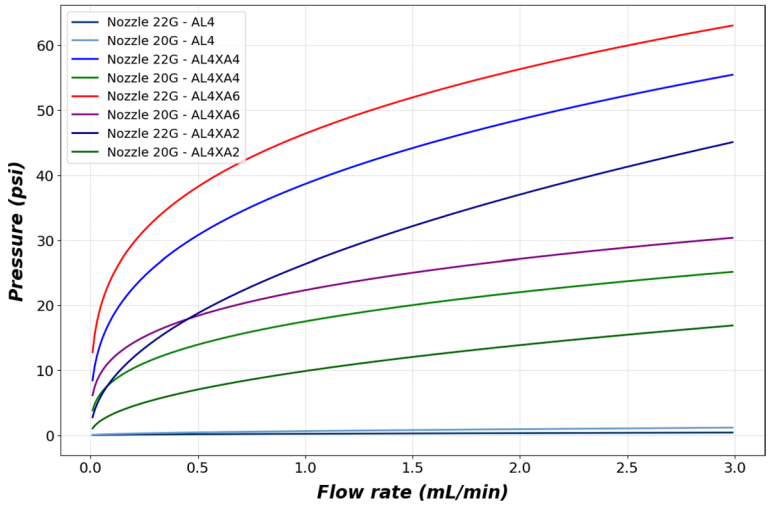

Fig. 4 Pressure as a function of flow rate for various formulations

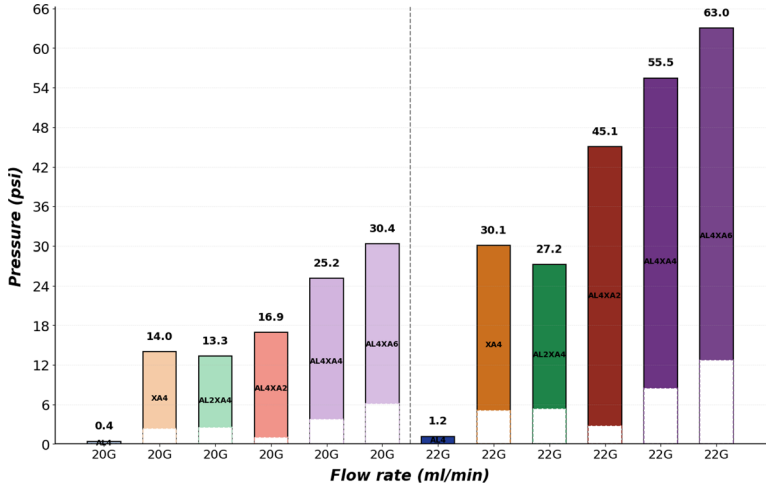

Fig. 5 Pressure required for different nozzle sizes and formulations

Figures 4 and 5 illustrate how smaller nozzle diameters demand significantly higher extrusion pressures, especially for formulations with higher xanthan gum concentrations, as exemplified by the AL4XA6 formulation requiring nearly double the pressure compared to AL4XA2 under the same flow rate; these findings emphasize the impact of K and n on extrusion performance, validate the predictive capabilities of the power-law model, and highlight its utility in optimizing extrusion parameters in bioprinting by anticipating the necessary pressures for specific material compositions and nozzle configurations, thus ensuring reliable

material flow and consistent deposition while reducing trial and error during process setup.

Rheological analysis: casson model evaluation

The rheological behavior of the AL4XA4 formulation was further evaluated using the Casson model (Equation 3), which provides insights into yield stress (τ_0) and plastic viscosity (η_0). The fitting yielded a yield stress of 187.17 Pa and a plastic viscosity of 0.59 Pa · s, with an excellent coefficient of determination ($R^2 = 0.95$). These parameters underline the formulation's significant resistance to flow initiation, critical for maintaining structural stability during extrusion-based 3D bioprinting.

The elevated yield stress highlights the material's ability to support multi-layered constructs without collapsing, while the high plastic viscosity ensures precise filament deposition and shape retention post-extrusion. The Casson model fitting, presented in Fig. 6, demonstrates the suitability of AL4XA4 as a yield stress ink, effectively minimizing deformation during bioprinting and enhancing reproducibility across various extrusion conditions.

The rheological characterization using the Casson model, which complements the findings from the oscillatory and flow sweep analyses, demonstrates that the yield stress (τ_y) reflects the minimum stress required to initiate material flow under continuous shear—critical for ensuring stable extrusion during bioprinting—while the gel point identified in the oscillatory amplitude sweep marks the transition from solid-like to liquid-like behavior ($G' = G''$) under oscillatory deformation, highlighting that yield stress ensures extrusion consistency and the gel point governs post-extrusion solidification [9, 21, 22].

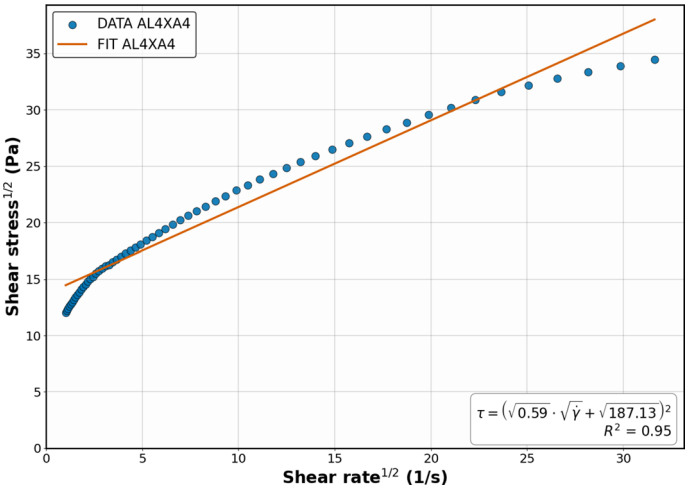

Fig. 6 Casson Model Fitting and Yield Stress Analysis for AL4XA4 ink, showing a yield stress of 187.17 Pa and plastic viscosity of 0.59 Pa · s, with a determination coefficient ($R^2 = 0.95$)

Oscillatory amplitude sweep and recovery behavior

Subjected to rheological characterization using an oscillatory amplitude sweep, the hybrid AL4XA4 gum bioink exhibited a transition from a solid-like to a viscoelastic state at a yield stress of 111.40 Pa, necessary for controlled extrusion, and as shear stress increased to 153.63 Pa, it demonstrated a sol–gel transition, maintaining structural integrity and ensuring stability under extrusion conditions.

The increase in the loss factor (tan δ) with applied shear stress suggests a shift toward viscous behavior, facilitating smoother extrusion and filament formation, which is crucial for reducing structural defects during biofabrication by preventing premature deformation and enabling continuous flow; as observed in other xanthan–alginate systems [9], where xanthan gum enhances elasticity at low shear stress and viscosity at higher stress levels, the hybrid formulation AL4XA4, compared to simpler alginate systems, shows a delayed transition to a viscous state, likely due to the synergistic interactions between alginate and xanthan gum, thus improving structural integrity during extrusion and being critical for high-fidelity bioprinting (Fig .7).

A step strain recovery test was conducted on a material, exposing it to a shear stress of 200 Pa for a duration of 10 s, which surpassed the sol–gel transition stress threshold. Demonstrating rapid elastic recovery, the material restores the predominance of the storage modulus over the loss modulus within approximately 0.55 s, signifying pronounced thixotropic properties that enable the bioink to swiftly re-solidify post-extrusion, recovering to around 300 Pa, which underscores its mechanical integrity for repeated bioprinting and aligns with xanthan–alginate

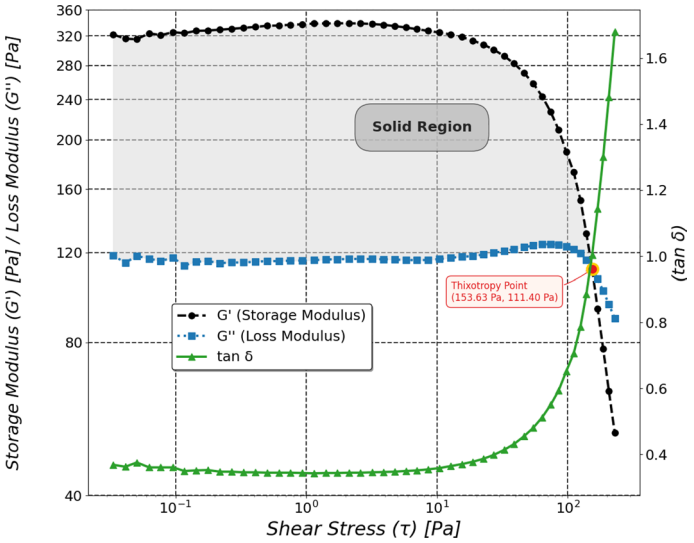

Fig. 7 Oscillatory amplitude sweep of AL4XA4. The graph illustrates the storage modulus (G') and loss modulus (G") as functions of increasing shear stress. The yield stress is identified at 111.40 Pa, followed by a sol–gel transition at 153.63 Pa, which is critical for the extrusion and structural integrity of the bioink

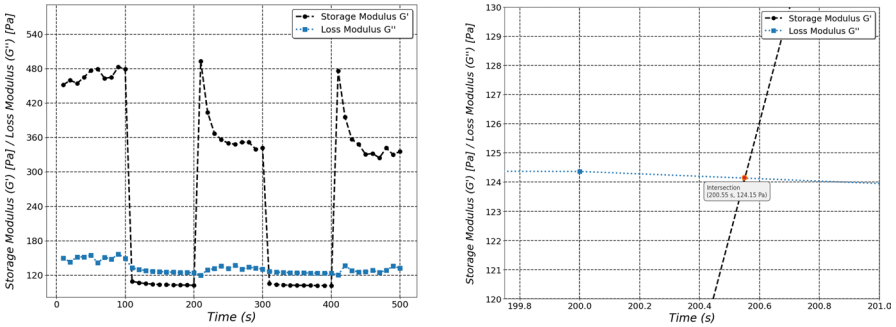

(a) (b)

Fig. 8 Step strain recovery test of the hybrid alginate–xanthan gum bioink. Panel **a** illustrates the recovery behavior after applying a shear stress of 200 Pa, while panel **b** zooms in on the recovery period between 190 and 210 s, demonstrating the material's fast recovery capability

systems where polymer interactions stabilize the hydrogel network. Furthermore, the AL4XA4 hybrid formulation, characterized by an elevated content of xanthan gum, exhibits accelerated recovery dynamics, underscoring the significance of xanthan in the immediate reorganization of the hydrogel matrix [9]. This attribute is advantageous for achieving precise, defect-free layer-by-layer bioprinting (Fig. 8).

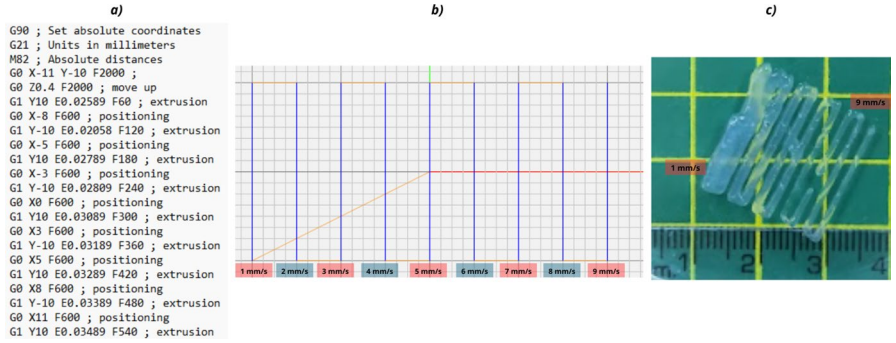

Fig. 9 **a** The G-code script enabled precise control over extrusion speeds for each printing line, ensuring uniform material deposition. Unlike conventional slicer software, which applies predefined global parameters, this approach allowed for a customized extrusion profile tailored to the rheological properties of the bioink. **b** The simulated trajectory visually represents the programmed variations in extrusion speed along the printing path, highlighting the gradual increase in velocity. **c** The experimental validation demonstrates the printed filaments at different speeds, showing a clear correlation between programmed speed and filament morphology

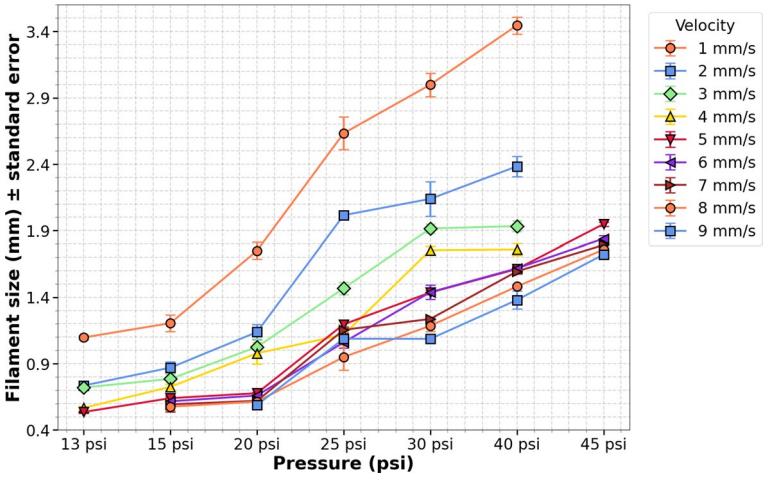

Fig. 10 Effect of extrusion pressure on filament size for AL4XA4 using a 22 G nozzle. Filament sizes range from 1.4 mm to 3.4 mm as pressure increases

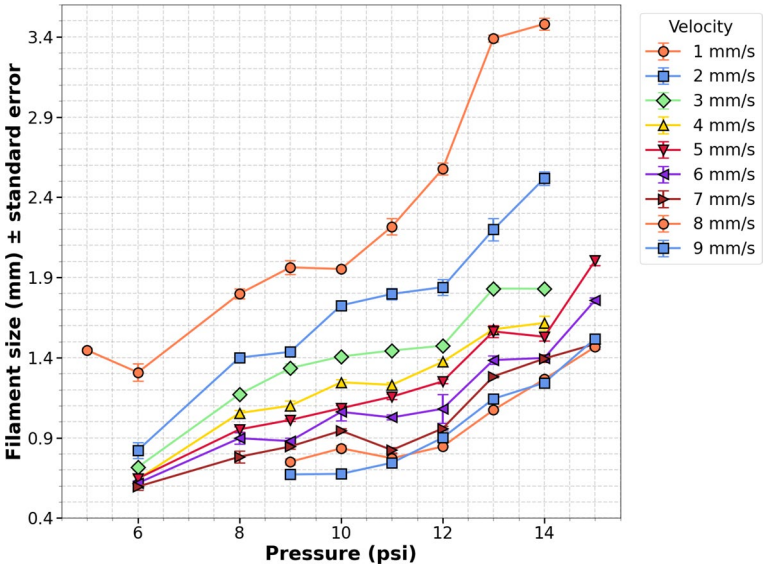

Fig. 11 Effect of extrusion pressure on filament size for AL4XA4 using a 20 G nozzle. Filament sizes range from 0.8 mm to 2.3 mm, showing similar behavior to the 22 G nozzle

Optimization of bioprinting parameters: impact on extrusion speed and resolution

Figure 9 illustrates the G-code model designed and simulated using the ncviewer online simulator. a) This G-code allowed precise control of extrusion speeds across

each printing line, ensuring uniform deposition. Unlike conventional slicer software, which relies on predefined global parameters, this approach allowed a customized extrusion profile tailored to the rheological properties of the bioink [29, 30]. Such precision was crucial for achieving consistent filament deposition, as validated experimentally.

The optimization process revealed a direct correlation between extrusion pressure, velocity, and nozzle size, confirming predictions from the rheological models. As shown in Figs. 10 and 11, smaller nozzles, such as 22 G, achieved higher resolution but required higher pressures to maintain consistent extrusion. Filament sizes for the 22 G nozzle increased linearly with pressure, ranging from 1.4 mm at 13 psi to 3.4 mm at 45 psi. In contrast, the 20 G nozzle exhibited a similar trend with larger filament sizes, ranging from 0.8 mm to 2.3 mm under the same pressure conditions. These findings validate the rheological predictions and highlight the role of pressure in determining print resolution.

Extrusion velocity also played a critical role in filament formation, as illustrated in Figs. 12 and 13. At low speeds (1–3 mm/s), overextrusion caused filament deformation and inconsistent sizes, particularly with smaller nozzles. At higher speeds (>7 mm/s), subextrusion resulted in incomplete deposition and structural discontinuities. Optimal conditions were observed at intermediate speeds, such as 9 mm/s, where filament sizes closely matched the theoretical range predicted by rheological models, with diameters decreasing to 0.9 mm for the 22 G nozzle and 0.6 mm for the 20 G nozzle.

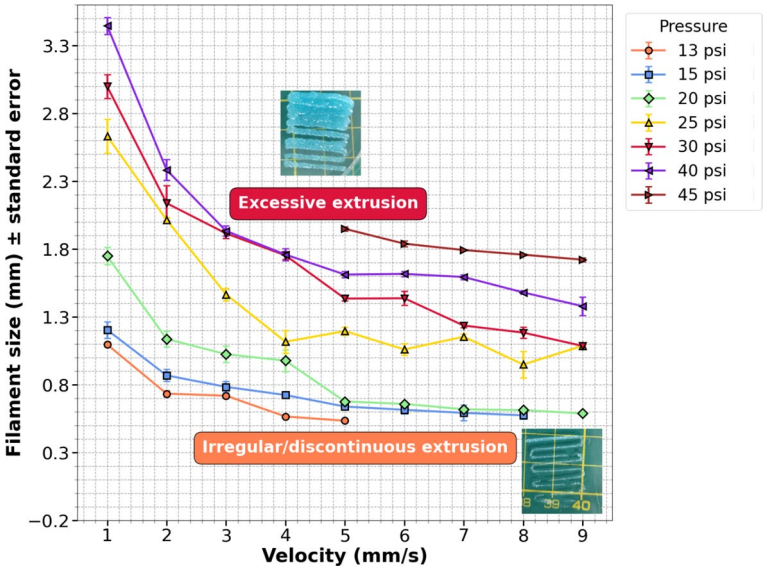

Fig. 12 Effect of extrusion velocity on filament size for AL4XA4 using a 22 G nozzle. Higher speeds produce finer filaments (down to 0.9 mm at 9 mm/s), although extreme speeds cause discontinuities and subextrusion

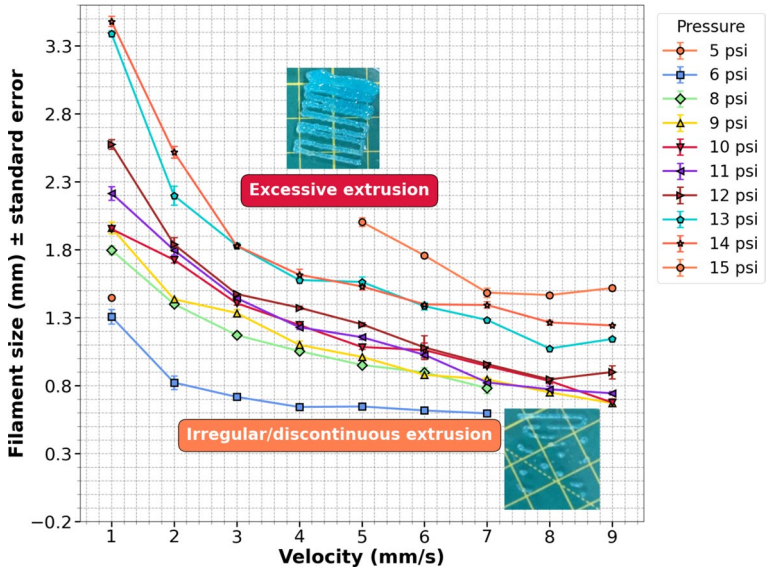

Fig. 13 Effect of extrusion velocity on filament size for AL4XA4 using a 20 G nozzle. The results show similar trends to the 22 G nozzle, although the larger nozzle allows more stable filament formation at higher speeds, reducing the risk of subextrusion

These findings align conceptually with the optimization framework presented by Belgin Paul et al. [51], where parametric analysis was employed to optimize extrusion parameters for β-TCP scaffolds. While both studies emphasize the importance of balancing speed, pressure, and nozzle size, the approaches differ in their methodologies. The Taguchi method used by Belgin Paul et al. leverages statistical optimization to identify robust parameter sets across variable conditions, providing versatility for a wide range of materials. In contrast, the pre-designed G-code in this study

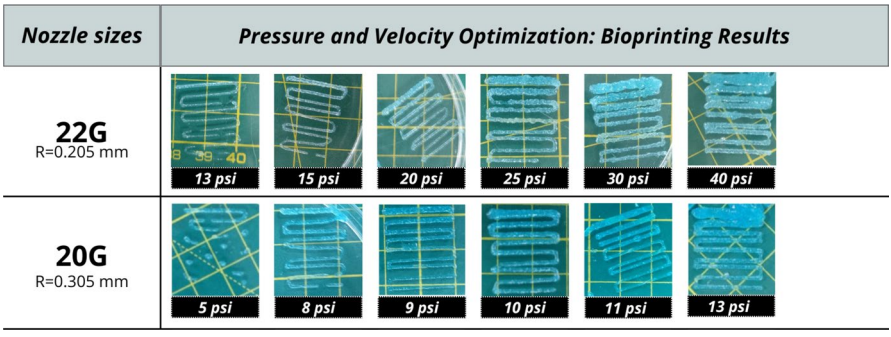

Fig. 14 Summary of the effects of varying pressures and velocities on filament formation using 22 G and 20 G nozzles. Optimal extrusion parameters are crucial for maintaining accuracy and avoiding overextrusion or subextrusion, particularly in small-scale structures

integrates rheological data to directly control extrusion parameters, ensuring fidelity under controlled conditions. Together, these approaches highlight complementary strategies for achieving high-dimensional accuracy in bioprinting.

Figure 14 summarizes the observed trends in extrusion fidelity, emphasizing the interplay between speed, pressure, and nozzle size. Overextrusion, prevalent at low speeds and high pressures, resulted in deformation and resolution loss. Subextrusion, occurring more frequently at higher speeds, led to insufficient deposition and structural weaknesses. These observations underscore the critical need for precise calibration of extrusion parameters to achieve consistent print quality.

Quantification of macropore geometry and circularity

A cross-hatched mesh was designed using G-code with a 90-degree rotation to determine the optimal macropore size and filament fusion condition. Macropores from 1 mm^2 to 4 mm^2 were generated, and PR was calculated diagonally for each macropore size to quantitatively evaluate the material's ability to preserve its geometry in a solid state [32, 33]. This experimental setup is demonstrated in Fig. 15.

As extrusion velocity increased to 240 mm/min and beyond, all macropore sizes (2x2 mm, 3x3 mm, and 4x4 mm) were successfully evaluated, showing noticeable improvements in precision and structural integrity. At these higher velocities, the Printability Ratio (PR) generally remained below 1 but within the optimal range (typically between 0.8 and 0.97), indicating sufficient extrudability while maintaining the intended geometry. The data revealed that increased velocity reduced filament size, resulting in more accurate macropore geometries and higher PR values, highlighting the critical role of velocity in enhancing resolution and fidelity (Fig. 16).

To explore the influence of pressure on print resolution, an additional experiment was conducted with a constant extrusion velocity of 360 mm/min. The extrusion pressure was systematically reduced to as low as 15 psi, while maintaining all other

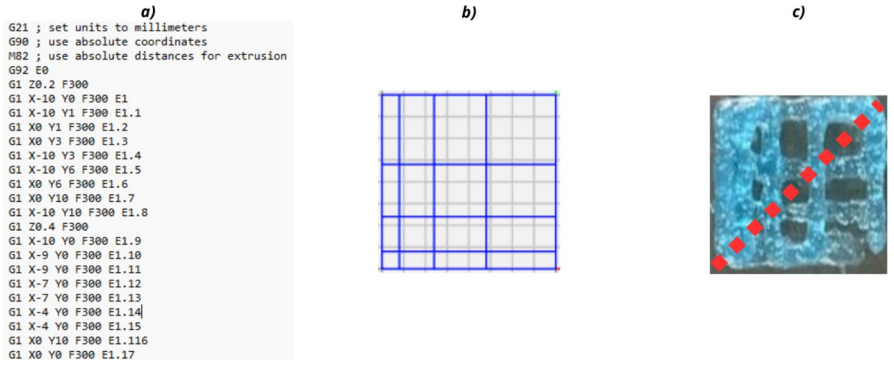

Fig. 15 **a** G-code script used to generate a cross-hatched mesh with a 90-degree rotation for macroporosity quantification. **b** Digital representation of the designed macropore structure. **c** Printed sample showcasing filament fusion and macropore formation, with PR calculated diagonally to assess structural integrity and printability

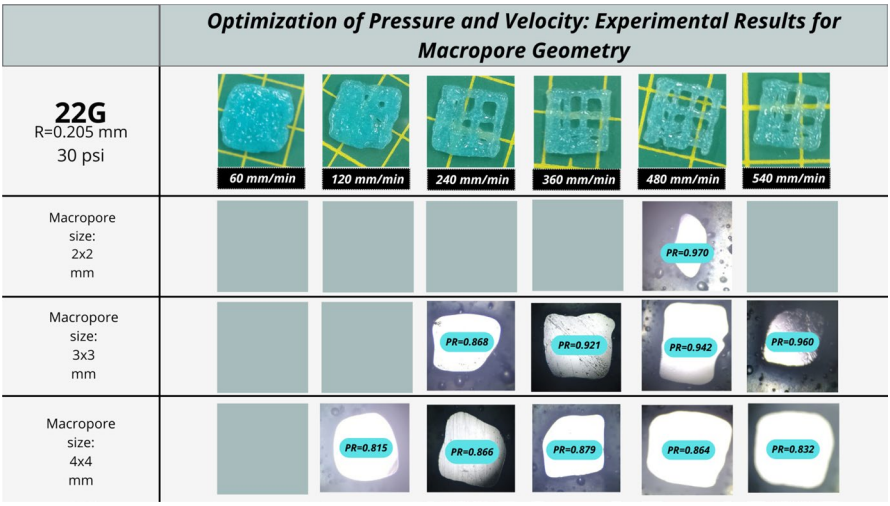

Fig. 16 Experimental results demonstrating the optimization of pressure and velocity on macropore geometry in DIW-printed hydrogel constructs using a 22 G nozzle. The figure highlights the impact of varying pressure and velocity settings on the Printability Ratio (PR) and the material's ability to maintain its designed macropore sizes, ensuring structural integrity and precision in the printed constructs

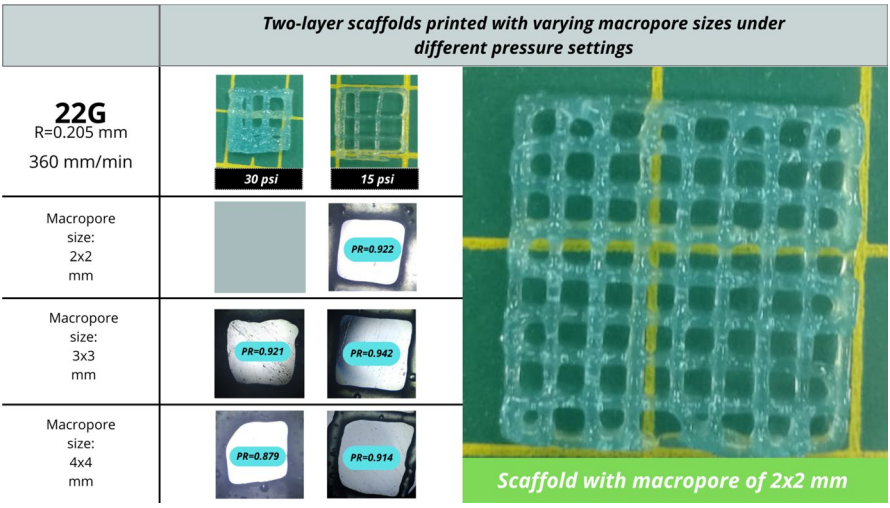

Fig. 17 Optimizing macropore formation at 360 mm/min yielded a 2x2 mm macropore at 15 psi, leading to the design of an 8x8 macropore mesh with improved resolution

conditions consistent with previous tests. This reduction in pressure led to a further decrease in filament diameter, enabling successful assessment of the 2x2 mm macropore, which was previously challenging under elevated pressure conditions. At a pressure of 15 psi, the 2x2 mm macropore achieved a PR of 0.922, demonstrating the material's capability to preserve its geometry with high fidelity. Building on

this, a comprehensive 8x8 macropore mesh was developed, representing a scaffold with optimal structural attributes for tissue engineering purposes (Fig. 17).

Evaluation of printability and structural stability

The printability of AL4XA4 ink was assessed by analyzing strand height (h_0) under varying extrusion conditions, focusing on gelation time (t_s) and structural stability. Smaller strands, such as those formed at 540 mm/s and 11 psi (0.680 mm), exhibited rapid gelation ($t_s = 0.037$ s), maintaining structural fidelity during extrusion. In contrast, larger strands, like those extruded at 1 mm/s (3.885 mm), gelled more slowly ($t_s = 0.212$ s), resulting in spreading and reduced print quality. Gelation time (t_s) was inferred from oscillatory amplitude sweep experiments, specifically from the point at which the storage modulus (G') exceeded the loss modulus (G''), indicating the transition from liquid-like to solid-like behavior.

Oscillatory amplitude sweep experiments supported these results, revealing a recovery time ($t_r = 0.55$ s) where the storage modulus (G') surpassed the loss modulus (G'') shortly after shear stress was removed. This rapid recovery underscores the material's ability to re-solidify effectively, enabling consistent layer-by-layer printing while minimizing structural defects. Together, these parameters emphasize the need to balance extrusion speed, pressure, and material properties to ensure print fidelity and structural cohesion.

Further analysis of the rheological properties demonstrated AL4XA4's capability to support multi-layered constructs. Using the yield stress ($\sigma_y = 153.63$ Pa), the theoretical maximum printable height ($h_{\max} = 9.32$ mm) was calculated. However, experimental observations revealed deformation at heights exceeding 3.89 mm, indicating the need for additional stabilization strategies, such as modified cross-linking techniques, to achieve reliable performance in taller constructs.

Self-supporting experimental setup

To evaluate the material's structural stability in unsupported spans, a custom platform was designed using Autodesk Fusion 360 and fabricated via fused deposition modeling (FDM) in PLA (Fig. 18). This experimental setup tested spans ranging from 1 mm to 6 mm under two distinct extrusion conditions to assess the hydrogel's inherent structural integrity prior to cross-linking.

Deformation was quantified using the Collapse Index (C_f), which was calculated for two conditions: high pressure and speed (15 psi, 360 mm/s) and low pressure and speed (11 psi, 60 mm/s). At higher pressure and speed, C_f remained below 5%

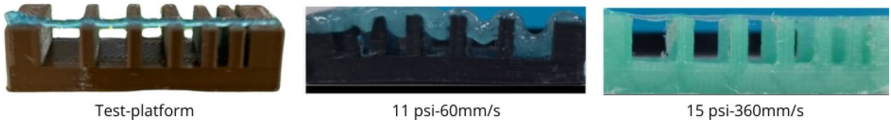

Fig. 18 Custom experimental setup designed in Fusion 360 and printed in PLA using FDM to evaluate the self-supporting capability of the AL4XA4 hydrogel across gap sizes (1–6 mm)

Table 3 Collapse Index (C_f) for different printing conditions. Values are expressed in percentage

Gap (mm)	C_f(**15psi**, **360mm/s**)[%]	C_f (11 psi, 60 mm/s) [%]
6	3.92	74.31
5	1.30	52.19
4	4.71	38.16
3	1.94	23.34
2	1.17	14.89
1	1.33	2.98

across all gap sizes, with minimal deformation (3.92%) observed at the largest span (6 mm). In contrast, at lower pressure and speed, C_f increased significantly, reaching 74.31% for the same gap size, as shown in Table 3. These results demonstrate that higher extrusion pressures and speeds effectively reduce sagging and maintain filament cohesion, ensuring structural stability in unsupported spans.

The AL4XA4 hydrogel successfully supported spans up to 6 mm without cross-linking, showcasing its inherent structural integrity under optimized extrusion conditions. These results align with prior studies [52], which highlighted the effectiveness of dual-cross-linking mechanisms in extending unsupported spans. Incorporating delayed cross-linking strategies could further enhance performance, enabling the fabrication of larger and more intricate geometries while maintaining print fidelity. It is worth noting that lower C_f values indicate reduced deformation and higher shape retention, making values closer to zero a desirable outcome when evaluating gravitational stability in self-supporting structures.

Chemorheological evaluation

The chemorheological analysis of the AL4XA4 hydrogel was conducted to evaluate the effects of ionic cross-linking with $CaCl_2$ on its mechanical stability and suitability for biomedical applications. Results demonstrated that increasing concentrations of $CaCl_2$ (1.5% and 3%) produced a significant increase in the storage modulus (G') and loss modulus (G''), indicating the development of a rigid external layer due to ionic cross-linking. This external layer maintained the geometry and functionality of the hydrogel during bioprinting, enabling it to support complex configurations essential for advanced applications. The rheological evolution during this cross-linking process is shown in Fig. 19.

These findings emphasize the role of controlled ionic cross-linking in optimizing hydrogel performance for bioprinting. This study demonstrated that the AL4XA4 hydrogel retains its structural integrity during post-extrusion processes. Furthermore, the synergistic effects of alginate and xanthan gum contribute to enhanced mechanical stability, as reported in prior studies [9].

Although the chemorheological evaluation focused on the AL4XA4 formulation, this assessment served as a representative model. The cross-linking behavior observed is expected to be applicable to the other hydrogel compositions tested

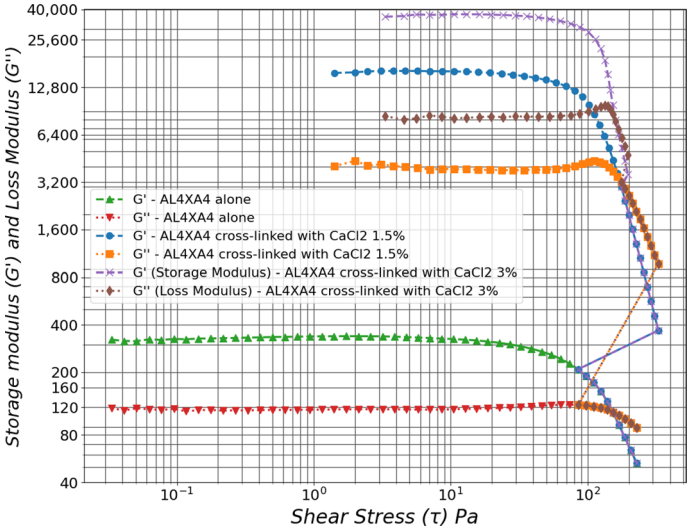

Fig. 19 Chemorheological analysis of AL4XA4 hydrogels cross-linked with varying concentrations of $CaCl_2$. The graph highlights the increase in G' and G'' due to ionic cross-linking

in this study, given their similar alginate–xanthan gum matrix and rheological characteristics.

While this study exclusively employed calcium chloride ($CaCl_2$) as the ionic cross-linker, recent findings suggest that the combined use of different divalent cations such as barium, magnesium, or strontium can further modulate the mechanical properties and gelation kinetics of hydrogels [53]. Incorporating these alternative cations could represent a promising route to enhance post-printing stability and

Fig. 20 Three-dimensional-printed ear model using AL4XA4 hydrogel cross-linked with $CaCl_2$, demonstrating its capacity to maintain structural integrity in complex geometries

should be considered for future hydrogel formulations based on this chemorheological framework.

The applicability of this cross-linking behavior was demonstrated through the fabrication of a 3D model of a human ear. The hydrogel was extruded in its uncross-linked state, followed by immediate post-extrusion cross-linking, which preserved its intricate geometry without collapse (Fig. 20).

This demonstration confirms the viability of the alginate–xanthan gum formulation as a structurally robust and printable hydrogel suitable for complex geometries. It is important to acknowledge that neither alginate nor xanthan gum possesses inherent cell-adhesive motifs. Consequently, future work could focus on enhancing the biological functionality of the system by incorporating components such as gelatin, whose intrinsic cell-binding motifs (e.g., RGD sequences) could promote cellular adhesion and integration[11]. This would enable the development of a next-generation hybrid hydrogel that combines structural integrity with bioactivity, addressing the dual requirements of mechanical performance and cellular interaction in tissue engineering applications.

Conclusion

This study establishes a systematic methodology for optimizing hybrid alginate–xanthan gum (AL4XA4) hydrogels for extrusion-based 3D bioprinting, integrating rheological and chemorheological characterization, predictive modeling, and experimental validation. This comprehensive approach addresses key challenges in achieving reproducibility, print fidelity, and structural stability, providing a robust framework for bioink development.

The rheological analysis revealed that AL4XA4 exhibits shear-thinning behavior with a consistency index ($K = 142.73$ mPa $\cdot$ s) and flow behavior index ($n = 0.33$) derived from the power-law model. These parameters were critical in predicting extrusion pressures and optimizing flow conditions for precise filament deposition. Oscillatory amplitude sweep tests identified a yield point at 111.40 Pa and a sol–gel transition at 153.63 Pa, essential for understanding the material's transition from solid-like to viscous behavior under shear. The Casson model further characterized the yield stress (187.17 Pa) and plastic viscosity (0.59 Pa $\cdot$ s), demonstrating the bioink's resistance to flow initiation and its capacity for maintaining structural integrity during extrusion.

Chemorheological analyses highlighted the impact of calcium cross-linking (1.5% and 3% $CaCl_2$) in enhancing mechanical stability and enabling unsupported spans up to 6 mm. This was validated through Collapse Index measurements, which confirmed minimal deformation ($< 5\%$) under optimized extrusion conditions. The bioink demonstrated excellent self-supporting capabilities and post-extrusion solidification, ensuring reproducibility in fabricating complex geometries. Additionally, predictive models were effectively integrated with custom G-code configurations to control extrusion speed and pressure, minimizing defects and achieving consistent macropore fidelity.

This work underscores the importance of integrating material science with process optimization to develop bioinks tailored for high-precision bioprinting. The methodology not only overcomes traditional trial-and-error approaches but also provides a foundation for advancing extrusion-based bioprinting techniques. Future directions include exploring adaptive hydrogel formulations responsive to biological environments, leveraging machine learning for predictive modeling, and expanding the framework to design scaffolds and drug delivery systems for clinically relevant applications in regenerative medicine.

Acknowledgements This work was funded by the Vicerrectorado de Investigación at the Pontificia Universidad Católica del Perú through grant DGI N°PI0985 and by the Consejo Nacional de Ciencia, Tecnología e Innovación Tecnológica – CONCYTEC – Perú (N°PE501078239-2022-Prociencia). The authors acknowledge the Maestría en Ciencia e Ingeniería de los Materiales at the Pontificia Universidad Católica del Perú for academic guidance and institutional support throughout the development of this work. The authors also thank the Laboratorio de Mecánica de Suelos at PUCP for granting access to the rotational rheometer used in the experimental phase of this research.

Funding Open access funding provided by Pontificia Universidad Catolica del Peru.

Data Availability The datasets generated, used, and/or analyzed during the current study are available from the corresponding author on reasonable request.

Declarations

Competing interests The authors declare that they have no competing interests.

References

1. Murphy SV, Atala A (2014) 3d bioprinting of tissues and organs. Nat Biotechnol 32(8):773–785
2. Agueda JRH Sta., Chen Q, Maalihan RD, Ren J, da Silva ÍGM , Dugos NP, Caldona EB, Advincula RC. (2021) 3d printing of biomedically relevant polymer materials and biocompatibility. MRS Commun 11(2):197–212
3. Gogoi D, Kumar M, Singh J (2024) A comprehensive review on hydrogel-based bio-ink development for tissue engineering scaffolds using 3d printing. Ann 3D Print Med 15:100159
4. Qavi I, Halder S, Tan G (2024) Optimization of printability of bioinks with multi-response optimization (mro) and artificial neural networks (ann). Progress Additive Manuf
5. Di Giuseppe M, Law N, Webb B, Macrae RA, Liew LJ, Sercombe TB, Dilley RJ, Doyle BJ (2018) Mechanical behaviour of alginate-gelatin hydrogels for 3d bioprinting. J Mech Behav Biomed Mater 79:150–157

6. Copus J, Lee SJ, Atala A (2022) Chapter 6 - bioink printability methodologies for cell-based extrusion bioprinting. In Lijie Grace Zhang, John P. Fisher, and Kam W. Leong, editors, *3D Bioprinting and Nanotechnology in Tissue Engineering and Regenerative Medicine (Second Edition)*, pp 153–183. Academic Press, second edition edition
7. Iberite F, Badiola-Mateos M, Loggini S, Paci C, Ruspi J, Iachetta D, Mannini A, Gruppioni E, Ricotti L (2024) 3d bioprinting of thermosensitive inks based on gelatin, hyaluronic acid, and fibrinogen: reproducibility and role of printing parameters. Bioprinting 39:e00338
8. O'Connell CD, Dalton PD, Hutmacher DW (2024) Why bioprinting in regenerative medicine should adopt a rational technology readiness assessment. Trends Biotechnol 42(10):1218–1229
9. Cofelice M, Messia MC, Marconi E, Cuomo F, Lopez F (2023) Effect of the xanthan gum on the rheological properties of alginate hydrogels. Food Hydrocoll 142:108768
10. Caceres-Alban J, Sanchez M, Casado FL (2023) Bioprinting: A strategy to build informative models of exposure and disease. IEEE Rev Biomed Eng 16:594–610
11. Pedroza-González Sergio C, Mario R-S, Pérez-Benítez Benjamín E, Alvarez Mariano M, Santiago Guillermo T (2021) Bioinks for 3d bioprinting: a scientometric analysis of two decades of progress. Int J Bioprint 7(2):333
12. Drury JL, Mooney DJ (2003) Hydrogels for tissue engineering: scaffold design variables and applications. Biomaterials 24(24):4337–4351
13. Leonardo M, Prajatelistia E, Judawisastra H (2022) Alginate-based bioink for organoid 3d bioprinting: A review. Bioprinting 28:e00246
14. Wani SUD, Ali M, Mehdi S, Masoodi MH, Zargar MI, Shakeel F (2023) A review on chitosan and alginate-based microcapsules: Mechanism and applications in drug delivery systems. Int J Biol Macromol 248:125875
15. Tajik S, Garcia CN, Gillooley S et al (2023) 3d printing of hybrid-hydrogel materials for tissue engineering: a critical review. Regen Eng Transl Med 9(1):29–41
16. Mukherjee K, Dutta P, Badwaik HR, Giri TK (2024) Chapter 6 - xanthan gum and its composite-based hydrogels. In Tapan Kumar Giri, Bijaya Ghosh, and Hemant Badwaik, editors, Polysaccharide Hydrogels for Drug Delivery and Regenerative Medicine, Elsevier. pp 89–108
17. James S, Moawad M (2023) Study on composite hydrogel mixture of calcium alginate/gelatin/kappa carrageenan for 3d bioprinting. Bioprinting 31:e00273
18. Ferreira KN, Girón JB, Gomes GHM, Rodas ACD, da Silva JVL, Daguano JKMB, Sabino MA (2024) Innovative thermosensitive alginate bioink combining cations for enhanced 3d extrusion bioprinting for tissue engineering. Bioprinting 39:e00340
19. Akkineni AR, Lode A, Gelinsky M (2024) 3d bioprinting of gelatin-alginate bioinks for biofabrication of in vitro liver sinusoid model. Procedia CIRP 125:96–100
20. Ramli H, Zainal NFA, Hess M, Chan CH (2022) Basic principle and good practices of rheology for polymers for teachers and beginners. Chem Teach Int 4(4):307–326
21. Herrada-Manchón H, Fernández MA, Aguilar E (2023) Essential guide to hydrogel rheology in extrusion 3d printing: How to measure it and why it matters? Gels 9(7):517
22. Rau DA, Bortner MJ, Williams CB (2023) A rheology roadmap for evaluating the printability of material extrusion inks
23. Muskan, Gupta D, Negi NP (2022) 3d bioprinting: Printing the future and recent advances. Bioprinting, 27:e00211
24. Montelongo SA, Chiou G, Ong JL et al (2021) Development of bioinks for 3d printing microporous, sintered calcium phosphate scaffolds. J Mater Sci Mater Med 32:94
25. Duty C, Ajinjeru C, Kishore V, Compton B, Hmeidat N, Chen X, Liu P, Hassen AA, Lindahl J, Kunc V (2018) What makes a material printable? a viscoelastic model for extrusion-based 3d printing of polymers. J Manuf Process 35:526–537
26. Gabriela Vaz and Luciano Silva. Parameterization of the e-value in g-codes for different bioprinters, 10 2023
27. Li X (2022) G-code re-compilation and optimization for faster 3d printing. In: Chapman B, Moreira J (eds) Languages and Compilers for Parallel Computing. volume 13149. Springer, Cham, pp 104–116
28. José Luis Dávila, Bruna Maria Manzini, Jéssica Heline Lopes da Fonsêca, Ingri Julieth Mancilla Corzo, Paulo Inforçatti Neto, Silmara Aparecida de Lima Montalvão, Joyce Maria Annichino-Bizzacchi, Marcos Akira d'Ávila, and Jorge Vicente Lopes da Silva. A parameterized g-code compiler for scaffolds 3d bioprinting. *Bioprinting*, 27:e00222, 2022

29. Gleadall A (2021) Fullcontrol gcode designer: Open-source software for unconstrained design in additive manufacturing. Addit Manuf 46:102109
30. Backes EH, Zamproni LN, Delgado-Garcia LM, Pinto LA, Lemes RMR, Bartolomeo CS, Porcionatto MA (2023) Protocol for designing and bioprinting multi-layered constructs to reconstruct an endothelial-epithelial 3d model. STAR Protoc 4(3):102467
31. Vajda J, Banović L, Miško M, Drstvenšek I, Milojević M, Maver U, Vihar B (2023) Algorithmic linearization improves syringe-based extrusion in elastic systems using hydrogel-based materials. Mater Des 229:111884
32. Ouyang L, Yao R, Zhao Y, Sun W (2016) Effect of bioink properties on printability and cell viability for 3d bioplotting of embryonic stem cells. Biofabrication 8(3):035020
33. Gillispie G, Prim P, Copus J, Fisher J, Mikos AG, Yoo JJ, Atala A, Lee SJ (2020) Assessment methodologies for extrusion-based bioink printability. Biofabrication 12(2):022003
34. Rau DA, Williams CB, Bortner MJ (2023) Rheology and printability: A survey of critical relationships for direct ink write materials design. Prog Mater Sci 140:101188
35. Pepper M, Cass C, Mattimore J, Burg T, Booth B, Burg K, Groff R () Post-bioprinting processing methods to improve cell viability and pattern fidelity in heterogeneous tissue test systems. *Conference proceedings : ... Annual International Conference of the IEEE Engineering in Medicine and Biology Society. IEEE Engineering in Medicine and Biology Society. Conference*, 2010:259–62, 08 2010
36. Afzali AM, Kheradmand MA, Naghib SM (2024) Bioreactor design-assisted bioprinting of stimuli-responsive materials for tissue engineering and drug delivery applications. Bioprinting 37:e00325
37. Alexandre D, Lucie E, Céline T, Emma P, Isabelle G, Magali B, Christophe M (2024) Confined bioprinting and culture in inflatable bioreactor for the sterile bioproduction of tissues and organs. Sci Rep 14(1):11003
38. O'Connell C, Ren J, Pope L, Zhang Y, Mohandas A (2020) Romane blanchard, serena duchi, and carmine onofrillo. Characterizing Bioinks for Extrusion Bioprinting: Printability and Rheology, Springer US, New York. pp 111–133
39. Li M, Tian X, Schreyer DJ, Chen X (2011) Effect of needle geometry on flow rate and cell damage in the dispensing-based biofabrication process. Biotechnol Prog 27(6):1777–1784
40. Chhabra RP, Richardson JF (2008) Non-newtonian flow and applied rheology. Butterworth-Heinemann, 2nd edition edition
41. Sun H, Kim Y, Kim YC, Park IK, Suhr J, Byun D, Choi HR, Kuk K, Baek OH, Jung YK, Choi HJ, Kim KJ, Nam JD (2018) Self-standing and shape-memorable uv-curing epoxy polymers for three-dimensional (3d) continuous-filament printing. J Mater Chem C 6(12):2996–3003
42. M'Barki A, Bocquet L, Stevenson A (2017) Linking rheology and printability for dense and strong ceramics by direct ink writing. Sci Rep 7(1):6017
43. Roussel N (2018) Rheological requirements for printable concretes. Cem Concr Res 112:76–85
44. Habib A, Sathish V, Mallik S, Khoda B (2018) 3d printability of alginate-carboxymethyl cellulose hydrogel. Materials (Basel) 11(3):454
45. Carvalho DN, Dani S, Sotelo CG, Pérez-Martín RI, Reis RL, Silva TH, Gelinsky M (2023) Assessing non-synthetic crosslinkers in biomaterial inks based on polymers of marine origin to increase the shape fidelity in 3d extrusion printing. Biomed Mater 18(5):055017
46. Li J, Zeng C, Huang Q, Zheng M-M, Chen J, Ma D (2023) Control release of α-mangostin by a novel dual-polysaccharides delivery system for colitis treatment under simulated gastrointestinal conditions. Food Biosci 53:102531
47. Sonaye SY, Ertugral EG, Kothapalli CR, Sikder P (2020) Extrusion 3d (bio)printing of alginate-gelatin-based composite scaffolds for skeletal muscle tissue engineering. Materials, 15(22)
48. He Y, Yang FF, Zhao HM, Gao Q, Xia B, JianZhong F (2016) Research on the printability of hydrogels in 3d bioprinting. Sci Rep 6(1):29977
49. Tuladhar S, Clark S, Habib A (2023) Tuning shear thinning factors of 3d bio-printable hydrogels using short fiber. Materials 16(2):572
50. Mrokowska MM, Krztoń-Maziopa A (2019) Viscoelastic and shear-thinning effects of aqueous exopolymer solution on disk and sphere settling. Sci Rep 9(1):7897
51. Belgin Paul DL, Praveen AS, Arjunan A (2025) Parametric optimisation for 3d printing β-tricalcium phosphate tissue engineering scaffolds using direct ink writing. Smart Mater Manuf 3:100070
52. Potere F, Venturelli G, Belgio B, Guagliano G, Boschetti F, Mantero S, Petrini P (2024) Double-crosslinked decm bioink to print a self-sustaining 3d multi-layered aortic-like construct. Bioprinting 44:e00368

53. Vajda J, Boštjan Vihar, Laura Činč Ćuri'c, Uroš Maver, Matej Vesenjak, Polona Dobnik Dubrovski, and Marko Milojević (2023) Sr2+ vs. ca2+ as post-processing ionic crosslinkers: implications for 3d bioprinting of polysaccharide hydrogels in tissue engineering. J Mater Res Technol, 23:1805–1820